High-speed tooth-coil permanent magnet synchronous machine for motorized spindle application

Zhu, Zichong; Ge, Wenjie; Deng, Jun; Dong, Jianning

DOI
10.3233/JAE-230006

Publication date
2024

Document Version
Final published version

Published in
International Journal of Applied Electromagnetics and Mechanics

International Journal of Applied Electromagnetics and Mechanics 75 (2024) 275–295
DOI 10.3233/JAE-230006
IOS Press

High-speed tooth-coil permanent magnet synchronous machine for motorized spindle application

Zichong Zhu[a,b,*], Wenjie Ge[a], Jun Deng[a] and Jianning Dong[c]
[a]*College of Electrical Engineering and Control Science, Nanjing Tech University, Nanjing, China*
[b]*Ningbo Shenglong Group Co., Ltd, Ningbo, China*
[c]*Department of Electrical Sustainable Energy, Delft University of Technology, Delft, The Netherlands*

Abstract. The slender shape of the driving machine leads to a low rigidity and large axial thermal elongation of the motorized spindle, which deteriorates the machining precision. To solve these problems and pursue a more compact size, this paper investigates the feasibility of using a tooth-coil permanent magnet synchronous machine in a high-speed spindle, replacing the original motor that has the conventional distributed winding. Comprehensive performance and behavior of machines with distributed and tooth-coil windings are comparatively analyzed, in terms of the essential torque ripples, winding inductances, electromagnetic losses, rotor integrity, and heat dissipation of the spindle. Thorough numerical simulation results indicate that the newly designed tooth-coil winding solution shows significant advantages over the original design, regarding high rotor rigidity, low torque ripples, reduced electromagnetic losses, and reduced shaft thermal elongation. Prototypes and test setups for the high-speed tooth-coil machine are built, where preliminary measurements are carried out to validate the analysis results and system design.

Keywords: Motorized spindle, electromagnetic loss, tooth-coil winding, permanent magnet synchronous machine, thermal elongation

1. Introduction

Owing to their high power density, high efficiency, and superior dynamic performance, permanent magnet synchronous machines (PMSMs) are widely used in motorized spindles [1]. Due to the limited switching frequency of power semi-conductors, pole numbers of spindle motors are usually 2, 4, or 6, depending on the operation speed. Meanwhile, the integral slot distributed winding is usually used in these machines. With short-pitch overlapped windings, the waveforms of the back electromotive force (EMF) and armature magnetomotive force (MMF) are significantly improved, which are considered to be beneficial for a low torque ripple and electromagnetic loss. However, high-speed PMSMs with distributed windings have slender rotors due to long end winding and a small split ratio [2]. This kind of rotor feature

*Corresponding author: Zichong Zhu, College of Electrical Engineering and Control Science, No. 30, Puzhu Road(S), 211816 Nanjing, China. Tel.: +86 17366010980; E-mail: zhu_zichong@njtech.edu.cn.

a low rigidity and a large axial thermal elongation [3], which have been recognized as the main barriers to higher machining precision. Additionally, the long end winding also hinders further miniaturization of the spindle.

PMSM with tooth-coil winding (TC-PMSM) is promising to solve these problems, considering their shorter end winding and larger rotor diameter. Nevertheless, TC-PMSMs are rarely used in high-speed applications [4], due to a larger number of poles and rich MMF harmonics [5]. It is expected that more loss will produce in TC-PMSMs than in its counterparts with distributed windings, including the stator iron loss, ac copper loss, rotor eddy current loss, and inverter high-frequency switching loss, due to a higher frequency and poorer MMF field [6]. Consequently, high-speed TC-PMSMs usually have a fractional HP power or less [7], and commonly utilize the 2-pole/3-slot or 4-pole/6-slot configurations, coming with low power density.

Owing to the development of high-band-width semi-conductor power devices, such as the SiC and GaN [8], the allowable switching frequency of the inverter is significantly enhanced. Accordingly, a higher operating frequency is achievable. In other words, high-speed TC-PMSMs with more poles than existing solutions can be considered. Another barrier that hinders the application of TC-PMSM is the increased loss density, caused by a higher frequency and rich MMF harmonics. Firstly, the increased frequency leads to a higher iron loss density in the stator core. To reduce this loss, various stator core materials are developed, such as ultra-thin silicon steel sheet [9], amorphous iron-based alloy [10], and soft magnetic composite. Moreover, a higher electromagnetic frequency inevitably exacerbates the uneven current distribution in conductors due to the skin effect, and more winding copper loss will be produced. To suppress it, a pre-formed rectangular winding is proposed for a 15000 r/min, 8-pole/12-slot TC-PMSM [11]. Similarly, round Litz wire is used for high-speed TC-PMSMs in [6], where the ac copper loss factor is largely reduced. Meanwhile, accurate conductor placement [13], hollow aluminum coils [14], and optimized stator [15] are also effective for reducing ac copper loss.

As for rotor eddy current loss, the key point is suppressing the MMF harmonics. Relevant researches aimed at this problem from multiple fronts include the stator yoke flux barriers [16], two-pitch coils [17], wye-delta hybrid connected windings [18], unequal teeth [19], multi-layer windings [20], various turns per coil side [21]. Meanwhile, measures on the rotor side are also proposed, such as the conducting sleeve [22], rotor flux barriers [23], rotor shape optimization [24], high-conductivity damping ring [25], low-conductivity sleeve [26], magnet lamination [8], and semi-magnetic IPM rotor [28].

In addition, according to the structure and loss distribution of TC-PMSM, new cooling methods are correspondingly proposed for the higher loss density, such as 3D printed ceramic slot heat exchanger [24], tooth-coil direct cooling [30], slot cooling ducts [31], and end-winding insert cooling [32]. By improving the heat dissipation, the speed/frequency boundary of TC-PMSM is greatly expanded.

In summary, the main barriers are removed gradually, and TC-PMSMs are promising in large-power high-speed applications, such as electric turbocharger, fuel-cell hydrogen compressor, and motorized spindle here. However, relevant cases are mainly in the concept design [11] or component development stages [24], but few have reported comprehensive design considerations, performance evaluation, and prototypes in application-intent motor design [8,26].

This paper presents the feasibility study of a 10-pole/12-slot TC-PMSM for a 12.5 kW, 15000 r/min motorized spindle, where a 6-pole/36-slot PMSM with distributed winding is currently installed. The main objectives of this paper are to elaborate characteristics of a high-speed PMSM with tooth-coil winding and reveal its potential for increasing the motorized spindle's rigidity, efficiency, and miniaturization. For this purpose, key performances of the benchmarked 6-pole/36-slot PMSM and newly developed 10-pole/12-slot TC-PMSM are comparatively investigated, in terms of output torque, inductance, losses,

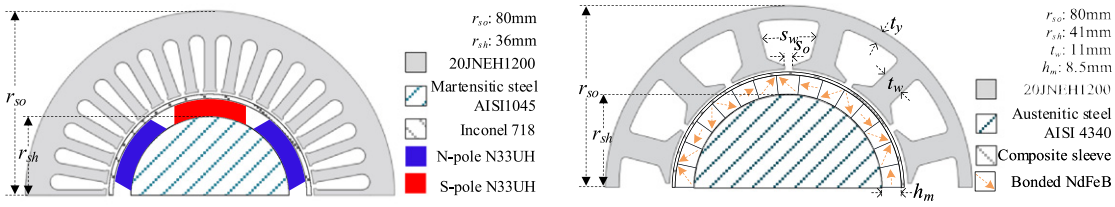

(a) 6P36S (b) 10P12S

Fig. 1. Dimensions and materials of the effective parts of the spindle motors.

Table 1
Design specifications of the 6P36S spindle motor

Parameter	Value	Parameter	Value
Rated power (kW)	12.5	Rated speed (r/min)	15000
Rated torque (Nm)	8.20	Magnet length (mm)	50
Stator stack length l_{stk} (mm)	50	Stator out radius r_{so} (mm)	80
Shaft radius r_{sh} (mm)	36	Air gap length (mm)	0.7

heat dissipation, and rotor strength. In addition, the manufactured prototypes and the experimental measurements are carried out to confirm the analysis results.

2. Specifications and parameters of the spindle motor

The motorized spindle equips with a 6-pole/36-slot PMSM (6P36S) that uses the surface-mounted arc-shaped magnets and short-pitched two-layer distributed winding, as shown in Fig. 1(a). The 6P36S is driven by an inverter with a 10 kHz switching frequency, and its main specifications are listed in Table 1. Due to the long end winding, 6P36S has a large axial dimension, which lowers the stiffness of the spindle. Consequently, severe resonance resulting from the overcritical operation is observed in some machining cases. Meanwhile, the long end winding is the main barrier to a more compact size and stator heat dissipation, which greatly influence the thermal elongation and machining precision of the spindle.

To solve these problems, a TC-PMSM with 10 poles and 12 slots (10P12S) is proposed to replace 6P36S, as in Fig. 1(b). Since non-overlapped tooth coils are used, 10P12S has shorter end winding, thereby a shorter axial length between the extremities of the end caps is resulted. For fair performance evaluations, 10P12S is designed with the same power, speed, and stator outer diameter as 6P36S. The winding parameters of these two machines are listed in Table 2, where the voltage limit requires two parallel paths for each phase winding. The current density of 10P12S equals that in 6P36S, to produce identical dc copper loss density. Also, the original 0.2 mm-thick silicon steel sheet 20JNEH1200 is kept in 10P12S, though with a higher frequency. As for the rotor assembly, surface-mounted magnets are continually used, considering spindle rigidity, but the original sintered NdFeB is replaced by bonded ones, to reduce the eddy current loss caused by rich MMF harmonics. Similarly, a sleeve made of carbon

Table 2
Winding parameters of 6P36S and 10P12S

Parameter	6P36S	10P12S
Coil pitch	5	1
Turns per coil	4	16
Number of parallel paths per phase winding	2	
Strands in hand per turn of coil	20	20
Copper diameter r_{co} (mm)	0.58	
Gross slot fill factor	0.38	
Rated current (Amplitude, A)	62.3	
Current density (A/mm^2)	4.17	
Phase resistance (Ω, 20 °C)	0.0151	0.0117

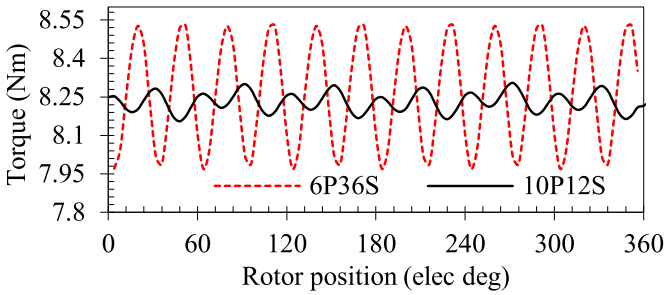

Fig. 2. Torque waveforms of 6P36S and 10P12S.

fiber composite is employed, which shows superiorities over a metallic one in the higher strength to weight ratio and higher electrical resistivity. Moreover, as the Halbach magnet array is utilized to increase the magnetic load, 10P12S has a rotor hub (spindle shaft) made of non-magnetic austenitic steel AISI4340, which has a higher strength than magnetic martensitic steel.

Detailed geometrical dimensions, such as the stator tooth width, yoke thickness, slot opening, split ratio, magnetization direction, and magnet thickness et al, are optimized using the genetic algorithm based on the 2D finite element method, where the single objective function is the highest efficiency under given output power and torque ripple constraints. The resultant optimal machine geometry is shown in Fig. 1(b). As with new windings and more poles, 10P12S has different performance metrics from 6P36S, and the forthcoming sections evaluate these two machines comparatively.

3. Torque output and inductance increment

As mentioned above, 10P12S is designed to output identical average torque as the original machine under the same current excitation, as presented in Fig. 2. It can be seen that 10P12S has a lower torque ripple, which owes to the reduced cogging torque after using the fractional slot winding scheme. Generally, the torque ripple decrement helps to improve the surface finishing quality of the workpiece.

Table 3
Line inductances and their components

Machine	L (μH)	L_{2d} (μH)	L_{ew} (μH)	L_g (μH)	L_σ (μH)
6P36S	88.04	67.45	20.59	37.18	30.27
10P12S	152.96	132.82	20.14	57.02	75.76

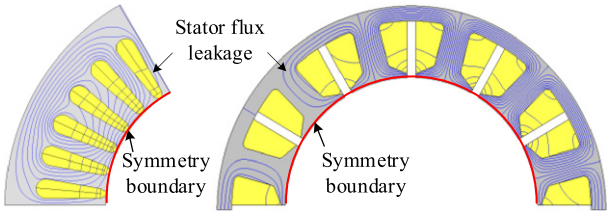

Fig. 3. Stator flux leakage calculated using symmetry boundary (Flux between two lines: 0.0002Wb).

The inverter that supplies the spindle motor consists of an output LC filter, to suppress the current harmonics and reduce relevant losses. However, it is the filter inductance that leads to a bulk inverter while lowers the efficiency and power factor. At the same time, loss in filter inductance challenges inverter heat dissipation. Therefore, to reduce filter volume and thermal load, a large machine inductance is preferred. Comparatively, with the tooth-coil winding, 10P12S has a larger line inductance than 6P36S which uses the distributed winding. Table 3 lists the calculated line inductance L using 3D finite element analysis (FEA) and its various components. It can be seen that though with a non-magnetic rotor hub, L of 10P12S reaches 152.96 uH, nearly twice that of 6P36S.

Each component of L is further separately analyzed, to reveal the reasons for its increment. The end winding inductance L_{ew} is derived by differentiating inductances calculated by 3D and 2D FEA [30]. Furthermore, inductance from 2D FEA L_{2d} is divided into the stator leakage inductance L_σ and the air-gap inductance L_g, as in (1).

$$L = L_{ew} + L_{2d} = L_{ew} + L_g + L_\sigma. \tag{1}$$

To separate L_σ and L_g, symmetry boundaries are imposed on the inner surface of the stator core, as shown in Fig. 3, to hinder armature flux from entering the air gap.

From Table 3, it was found that both L_σ and L_g are increased, by using the tooth-coil windings. Whereas, L_{ew} of these two machines are quite close. The reason for a larger L_σ in 10P12S is that more stator flux leakage produces, as shown in Fig. 3, due to a smaller coil pitch when excited by the same current. As for the increment of L_g, the contribution is the rich MMF harmonics, and the inductance corresponding to these harmonics is referred to as the harmonic leakage inductance. Of course, the larger inductance and higher frequency in 10P12S produce a lower power factor, which declines from 0.99 to 0.91 after using the tooth-coil winding, but this decrement is negligible and has a minor influence on inverter capacity.

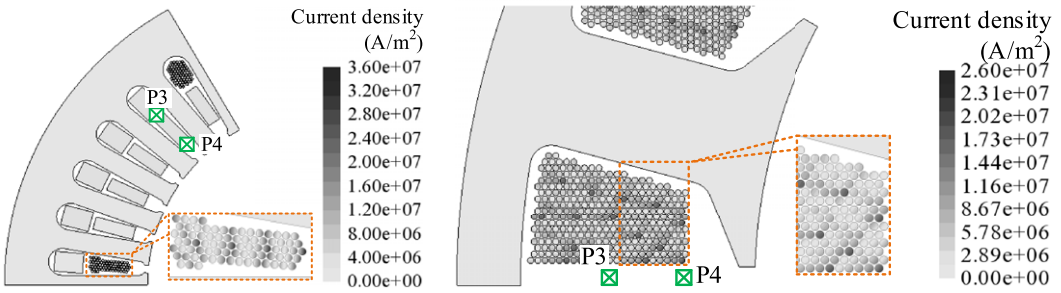

(a) 6P36S (b) 10P12S

Fig. 4. Current densities in the conductors of the slot winding at 1250 Hz.

4. Electromagnetic losses and their distribution

4.1. Winding copper loss

As mentioned above, some winding parameters of 10P12S and 6P36S are designed identical, including the strands in hand per turn of coil, conductor diameter, gross slot fill factor, and dc current density. Whereas, due to a longer end winding and more slots, 6P36S has a larger phase resistance, as shown in Table 2. Accordingly, 10P12S is expected to have a smaller copper loss. However, it deserves to note that the fundamental frequency of 10P12S increases from 750 Hz to 1250 Hz, which inevitably produces a larger ac copper loss due to the uneven current distribution caused by the skin effect.

To calculate the ac copper loss P_{ac}, conductors in a coil are directly modeled in 2D FEA, where uneven current distribution can be considered. Figures 4 and 5 present the current densities in slot and end windings at the rated point. Due to the skin effect, the maximum current density $J_{\max}$ in slot winding of 10P12S is 26.53 A/mm^2, far larger than the dc value of 4.17 A/mm^2. In the end winding, $J_{\max}$ reaches 9.98 A/mm^2. Comparatively, $J_{\max}$ in slot and end windings of 6P36S are 35.7 A/mm^2 and 9.88 A/mm^2, respectively.

It can be concluded that $J_{\max}$ in end winding of 10P12S is close to that of 6P36S. Whereas things are different for the slot winding, whose $J_{\max}$ is far smaller than its counterpart in 6P36S. The main reason is that by using the tooth coil winding, the slot width increases. Consequently, slot flux leakage and resultant current uneven distribution are suppressed. Figure 6 presents flux densities in the slot center and slot top on load condition, where the sampling points P3 and P4 are shown in Fig. 4. It was found that both the radial and tangential components of the slot magnetic field are largely reduced, by a wider slot. As a result, though with a higher current frequency, the maximum current density in slot winding of 10P12S is instead reduced.

Table 4 lists the calculated P_{ac} in different winding parts, where the loss in end winding is calculated using the predicted end winding length and current density from 2D FEA. The ac copper loss factor k_{ac}, is given by (2), where P_{dc} is the dc copper loss according to phase resistance. From Table 4, k_{ac} of 10P12S is indeed increased, from 1.24 to 1.45 due to a higher frequency, but the increment is far less than the square of the variation of f. The relatively small increment attributes to the lower magnetic field in the stator slot, as shown in Fig. 6. In addition, it is noteworthy that by using the tooth-coil winding, 10P12S has an unexpected copper loss reduction, from 109.23 W to 98.4 W. This reduction owes to the shorter

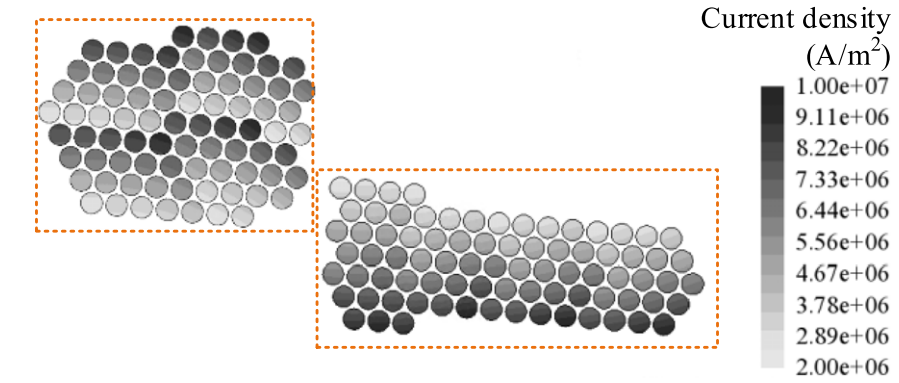

(a) 6P36S

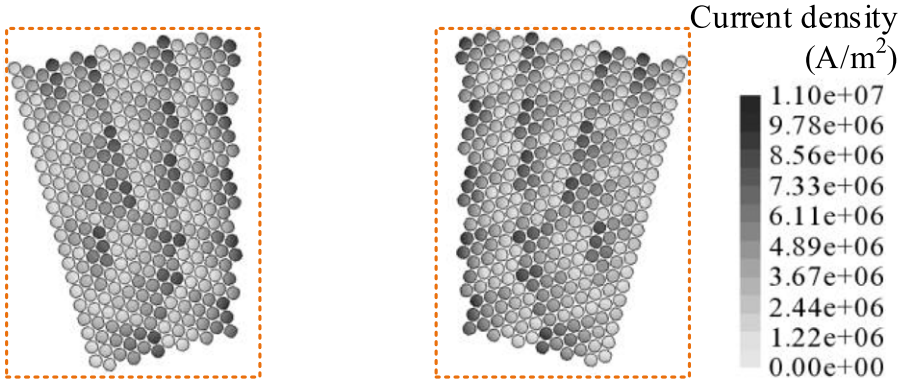

(b) 10P12S

Fig. 5. Current densities in the conductors of the end winding at 1250 Hz.

end winding of 10P12S and its lower dc copper loss.

$$k_{ac} = \frac{P_{ac}}{P_{dc}}. \tag{2}$$

4.2. *Stator iron loss*

The stator iron loss P_{Fe} also increases with higher frequency f, according to Steinmetz equation (3). As with a larger number of poles, 10P12S is expected to have more loss in stator core than 6P36S, though they are designed with the same stator core material and close magnetic flux densities, as shown in Fig. 7.

To evaluate the variation of P_{Fe}, an FEA-based specific loss method is used. By this method, magnetic flux density in each element is obtained and its components $B_x \sim B_z$ are decomposed into Fourier series. P_{Fe} in each element is then calculated using tested iron loss coefficients k_h and k_e. For saving computation resources, harmonics with orders higher than 11 are ignored. By suming losses in all m elements, the total

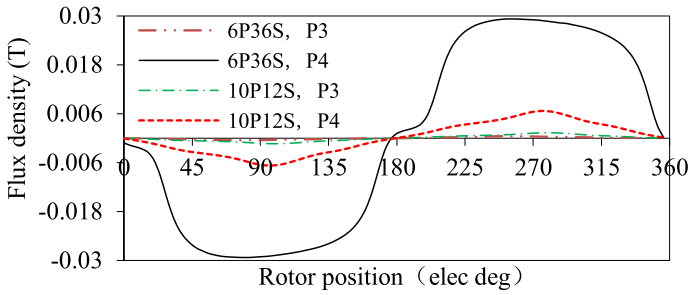

(a) Radial component

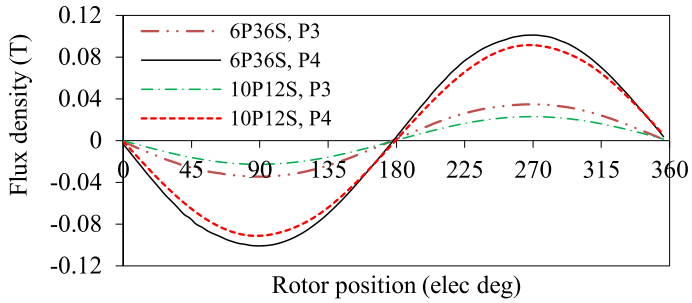

(b) Tangential component

Fig. 6. Magnetic flux densities in stator slot.

Table 4
Winding copper loss of 6P36S and 10P12S

Machine	P_{dc} (W)	P_{ac} in end winding (W)	P_{ac} in slot winding (W)	P_{ac} (W)	k_{ac}
6P36S	87.62	50.62	58.61	109.23	1.24
10P12S	67.93	25.51	72.89	98.4	1.45

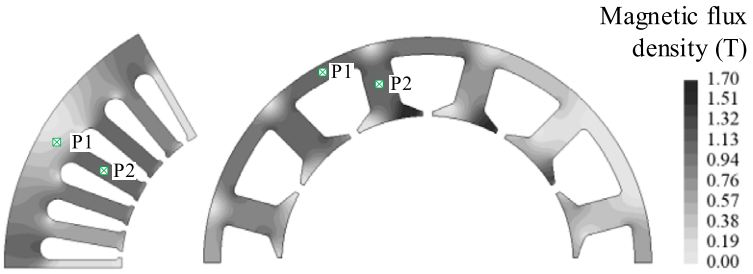

Fig. 7. Magnetic flux densities in stator core on load condition.

Table 5
Stator iron loss of 6P36S and 10P12S

Machine	Hysteresis loss P_h (W)	Eddy current loss P_e (W)	P_{Fe} (W)
6P36S (open circuit)	95.61	118.19	213.80
6P36S (rated load)	97.49	120.46	217.95
10P12S (open circuit)	64.55	108.28	172.84
10P12S (rated load)	76.07	130.58	206.65

P_{Fe} is calculated, as in (4), where V_j is the volume of the jth element, and f_ν is the frequency of the νth harmonic.

$$P_{Fe} = P_h + P_e = k_h f B_m^{cfa} + k_e f^2 B_m^2 \tag{3}$$

$$P_{Fe} = P_h + P_e = \sum_{j=1}^{m} \sum_{\nu=1}^{11} V_j \left[k_h f_\nu \left(\sqrt{B_{x\nu}^2 + B_{y\nu}^2 + B_{z\nu}^2} \right)^{cfa} \right] + \sum_{j=1}^{m} \sum_{\nu=1}^{11} V_j [k_e f_\nu^2 (B_{x\nu}^2 + B_{y\nu}^2 + B_{z\nu}^2)]. \tag{4}$$

Table 5 lists the calculated P_{Fe} and its components on the open-circuit and load conditions. In these two machines, the on-load and open-circuit P_{Fe} have little difference, particularly in 6P36S, because they are designed with relatively low electrical loads, to lower the temperature gradient in the spindle housing. Therefore, the armature magnetic field is subordinate to the magnet field, which explains the minor iron loss difference on open-circuit and load conditions.

It can also be seen from Table 5 that in contrast with estimation, 10P12S has a smaller iron loss than 6P36S, despite a higher frequency. Two reasons account for this phenomenon, and one is the reduced stator core usage. In the new design, the stator tooth and yoke are downsized due to more poles and a larger stator split ratio, which contribute to a 32.8% decrement of the stator core, from 3.72 kg to 2.50 kg. Another reason is the more sinusoidal magnetic field in the stator core. Figure 8 presents the radial and tangential flux densities in stator tooth and yoke, and the sampling points are shown in Fig. 7. It was found that the stator magnetic field in 6P36S contains rich harmonics. Whereas, in 10P12S, the stator magnetic field are approximately sinusoidal. Figure 9 shows P_{Fe} caused by each harmonic using (4), where loss corresponding to the 3rd, 5th, and 7th harmonics are reduced in 10P12S. Consequently, though the fundamental produces more loss,10P12S still outperforms 6P36S in terms of stator iron loss.

In addition, it deserves to note that in 10P12S, the proportion of eddy current loss is larger than that in 6P36S, due to a higher frequency. Therefore, to further reduce P_{Fe}, the material with lower eddy current loss should be exploited, such as the 0.1 mm-thick silicon steel sheet and amorphous alloy.

4.3. Rotor eddy current loss

As discussed in Section 2, to reduce rotor eddy current loss P_{ed}, a low-conductivity composite sleeve and bonded NdFeB magnets are used in 10P12S. Meanwhile, non-magnetic steel, rather than permeable one, is selected for the rotor hub, considering its high resistivity. Table 6 shows the calculated P_{ed} by 3D

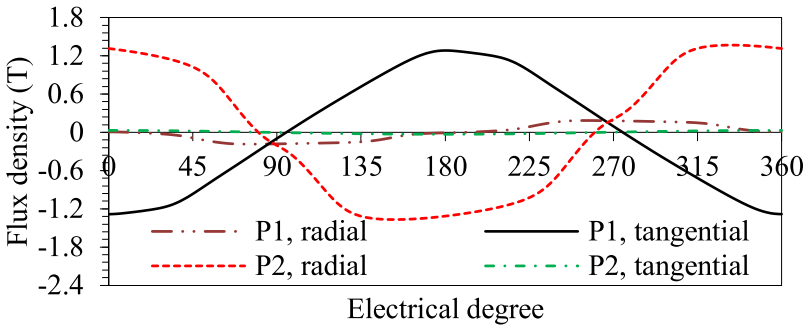

(a) 6P36S

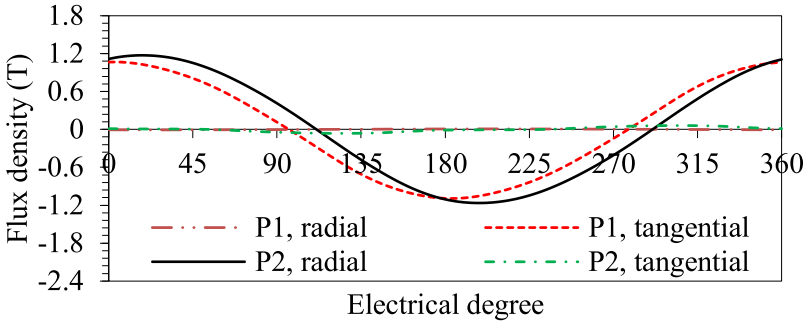

(b) 10P12S

Fig. 8. Magnetic flux density in stator tooth and yoke.

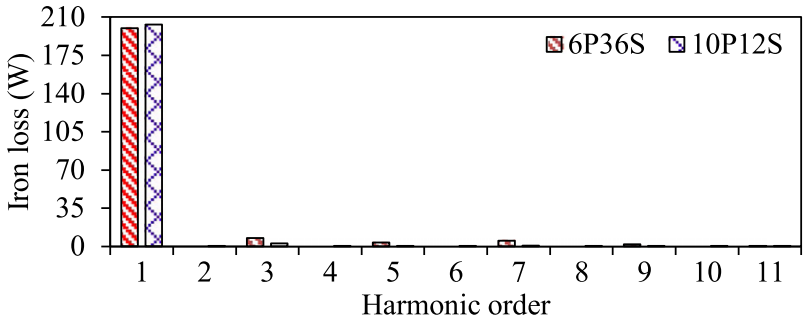

Fig. 9. Stator iron loss caused by each harmonic.

FEA and its distribution in each rotor part. By using the low-conductivity sleeve and magnet, 10P12S has a smaller P_{ed} than 6P36S, albeit with rich MMF harmonics. Furthermore, the majority of rotor eddy current loss in 6P36S appears in the metallic sleeve, implying that the harmonics hardly enter the rotor hub due to their high frequency and the magnetic shielding effect. However, things are different for 10P12S, its armature MMF harmonics have relatively low frequencies, especially the subharmonics, and thus larger skin depths. These harmonics penetrate the rotor hub and produce a large eddy current loss there, as illustrated in Fig. 10.

Table 6
Rotor eddy current loss of 6P36S and 10P12S

Machine	Sleeve (W)	Magnet (W)	Rotor hub (W)	Total eddy current loss P_{ed} (W)
6P36S	57.46	4.06	0.01	61.53
10P12S	12.44	0.04	31.3	43.78

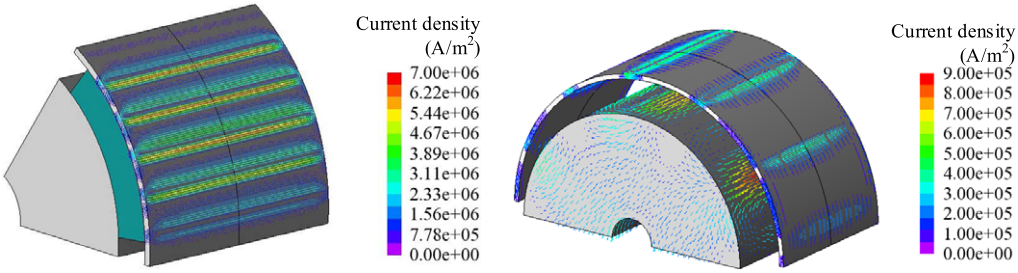

(a) 6P36S (b) 10P12S (magnets are hided)

Fig. 10. Rotor eddy current density on load condition.

Although the low-order MMF harmonics produce a large loss in the rotor hub, the total eddy current loss is still decreased by 28.85%, after using the tooth-coil solution. Meanwhile, rotor loss of 10P12S distributes more adjacent to the spindle shaft cooling fluid, which lowers rotor temperature rise and thermal elongation, as discussed in the next section.

5. Temperature rise and rotor strength evaluation

5.1. Temperature rise and thermal elongation

From the above analysis, electromagnetic losses of 10P12S are quite close to that of 6P36S. Whereas, since the machine topology and materials are changed, 10P12S shows various temperature rise levels and thermal behavior. FEA is used to calculate the temperature field, as in Fig. 11. As 10P12S has an identical stator out diameter with 6P36S, the housing jacket with spiral oil-cooling duct is retained. In the motorized spindle, the rotor is designed with a circular duct for the cooling purpose, where the cutting fluid flows through. To enhance its heat transfer ability and reliability, the winding is strengthened by vacuum impregnated epoxy resin SILRES H-62 and then potted using thermal conductive epoxy-based material EX5695 A.

In the thermal FEA model, contact thermal resistances between adjacent parts are considered using equivalent air gaps, which are determined according to [31–33]. Similarly, the bearing interface and slot liner are not directly modeled and their thermal resistances are represented by contact resistances, as well. For example, thermal resistance between the inner and outer races of the bearing is considered using a 0.18 mm air gap. In addition, to reduce the number of elements, the conductor, insulation varnish, and impregnation are modeled as a single part, i.e., the winding part in Table 7. This compound part

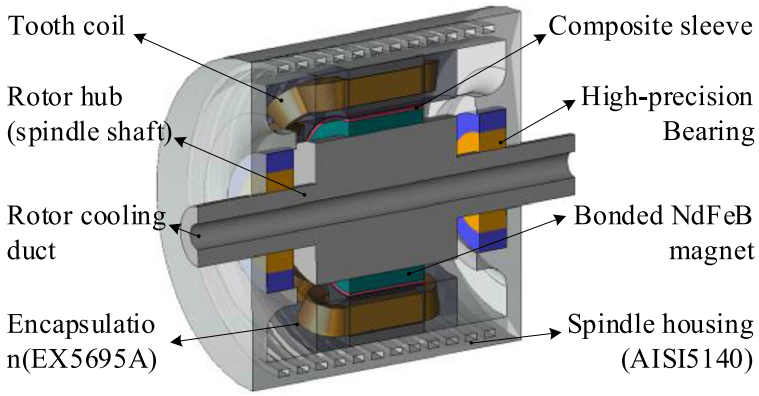

Fig. 11. Thermal FEA model of the motorized spindle with tooth coils.

Table 7
Thermal conductivity of the orthotropic parts

Part	Main axis (W/m/K)	Plane normal to the main axis (W/m/K)
Winding	348.7	3.18
Stator lamination	5.93	30.0
Sleeve	50.6	1.463

has transversely orthotropic properties. For example, its thermal conductivity along the current flowing direction is higher than that in the normal plane. Cases for the laminated stator core and composite sleeve are similar, whose main axes are the axial and circumferential directions, respectively.

A two-way coupled analysis is carried out, to consider the effect of temperature rise on electromagnetic performance. The average convective heat transfer coefficients, such as that in the housing cooling duct, encapsulated end winding to end space, rotor fluid cooling duct, and windage loss are imported from early-stage computational fluid dynamic (CFD) analysis, which are 1966.7 W/m^2/K, 35.71 W/m^2/K, 2254.1 W/m^2/K, and 89.63 W, respectively. Figure 12 shows the calculated temperature assuming the ambient and coolant temperatures at 55 °C. The maximum stator temperature is 87.5 °C. The hot spot appears in the end winding, which has a poor heat dissipation ability than the slot winding. In 6P36S, this value is 101.82 °C. Accordingly, the maximum winding temperature rise of 10P12S decreases by 14.32 °C, owing to a shorter end winding and reduced stator loss. As for the rotor, a smaller temperature rise is also obtained, for the smaller sleeve and magnet losses that are transferred to the rotor cooling fluid via two large thermal contact resistances, as shown in Fig. 13. Moreover, Table 6 indicates that by using low-conductivity sleeve and magnet, the rotor eddy current loss is “shifted” to the rotor hub that is directly cooled by cutting fluid, without undesirable contact resistances. Hence, the “loss shift” also contributes to a lower rotor temperature. In summary, high reliability can be expected since the lifetime nearly doubles when the spindle’s temperature decreases by 10 °C.

In the original design, the maximum axial thermal expansion of the spindle shaft is 0.29 mm. To enhance the machining precision and avoid unequal elongation of the rotary and stationary parts, axial

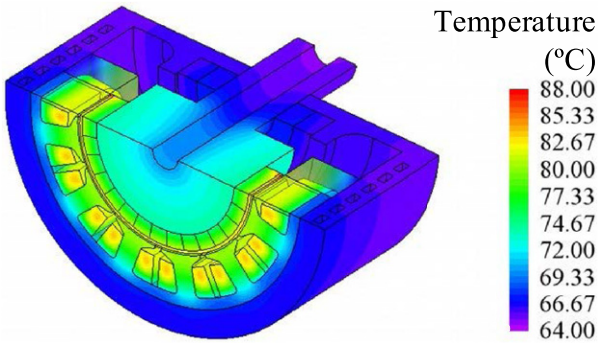

Fig. 12. Temperature distribution at the rated point.

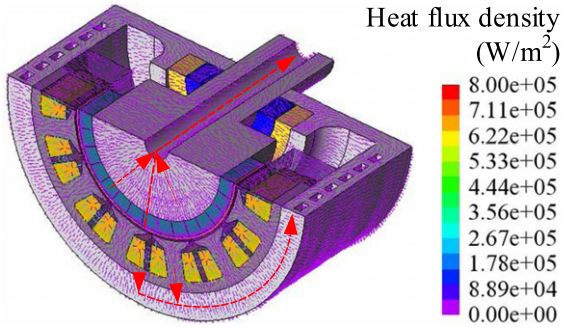

Fig. 13. Vector plot of heat flux with a 55 °C cutting fluid.

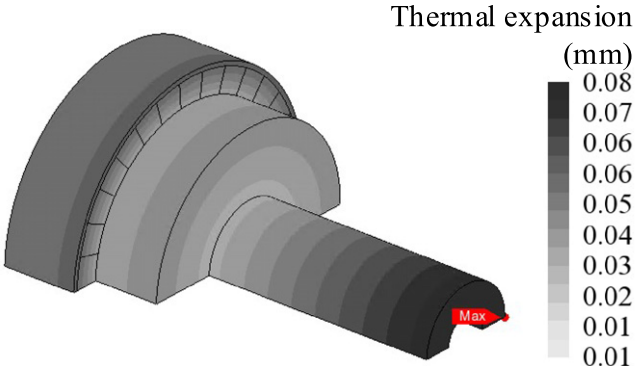

Fig. 14. Thermal expansion of the spindle rotor when using 10P12S.

thermal expansion is expected to be less than 0.20 mm. Figure 14 shows the thermal expansion of the spindle rotor when using 10P12S, where the maximum axial expansion is significantly reduced to 0.16 mm which fulfills the requirement. From Fig. 12, a high temperature gradient presents mainly in the spindle shaft, which leads to a large axial thermal expansion. Therefore, it is the downsized rotor dimension due to shorter end winding and reduced rotor loss that contribute to the decrement of thermal expansion.

5.2. Rotor strength evaluation

Unlike sintered ones, bonded magnets have low tensile and compressive strength simultaneously. For bonded NdFeB used in 10P12S, the allowable compressive and tensile strengths are merely 110 MPa and 37.2 MPa, respectively. Therefore, strength criterion is imperative for rotor design with bonded magnets. To calculate rotor stress and evaluate its integrity, structural 3D-FEA is used. The load from interference fit, centrifugal force, and thermal stress due to temperature gradient and various thermal properties are considered.

The spindle motor is operated with frequent start-stop, and rotor strength should be evaluated under various conditions. Three typical conditions are considered:

(I) Static rotor with on-load steady-state temperature, in this case, the interference fit and thermal stress work;
(II) Rotational rotor (20% over speed) at on-load steady-state temperature, where interference fit and centrifugal force are counted;
(III) Rotational rotor at steady-state temperature, where all three forces are covered.

Von Mises stress criterion is used to evaluate the strength of the rotor hub. From Fig. 15, the maximum Mises stress occurs when all three forces work together on Condition III, and reaches 69.51 MPa, which is far below the 0.2% yield strength of 407 MPa. For carbon fiber composite sleeve, the global stress is compared to the ultimate tensile strength, as in (5). Likewise, tangential normal stress σ_θ has a maximum value of 141.53 MPa on Condition III, as in Fig. 16, providing a safety margin of 3.11 with the measured tensile strength σ_{ts} at 441.3 MPa.

$$\sigma_\theta \leq \sigma_{ts}. \tag{5}$$

For bonded magnets, the first principal stress σ_1 and third principal stress σ_3 are calculated, and then compared with its tensile strength σ_{tm} and compressive strength σ_{cm}, as in (6). Figures 17 and 18 present their distributions. σ_1 has a maximum value of 18.5 MPa on Condition III, where the maximum value of σ_3 (absolute value) is 63.5 MPa. As σ_{tm} and σ_{cm} are 37.2 MPa and 110 MPa respectively, wide safe margins are designed for magnet strength.

$$\begin{cases} \sigma_1 \leq \sigma_{tm} \\ \sigma_3 \leq \sigma_{cm}. \end{cases} \tag{6}$$

6. Prototype and experimental validation

Two sleeves are developed, as shown in Fig. 19. One directly winds tensed carbon fiber filament onto the rotor with mounted magnets, and is cured using epoxy resin. Another is pre-formed using a mandrel mold and compressed onto the rotor, forming a 0.05 mm interference fit. However, it is found that the magnets are cracked during compression. Therefore, in the rotor prototype, the filament directly wound process is used.

The fabricated stator and setups for the static torque test are shown in Fig. 20. Phase resistance and inductance are measured and listed in Table 8. The line inductances are measured using a LCR meter and the result agrees well with the simulated one with the maximum error of 4.57%, confirming the correctness of winding fabrication. However, the measured resistance shows an obvious discrepancy with

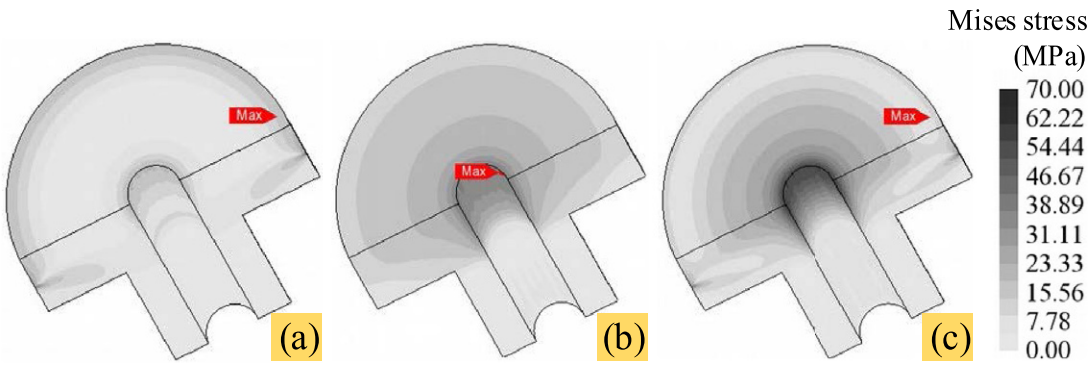

Fig. 15. Mises stress in rotor hub. (a) Condition I. (b) Condition II. (c) Condition III.

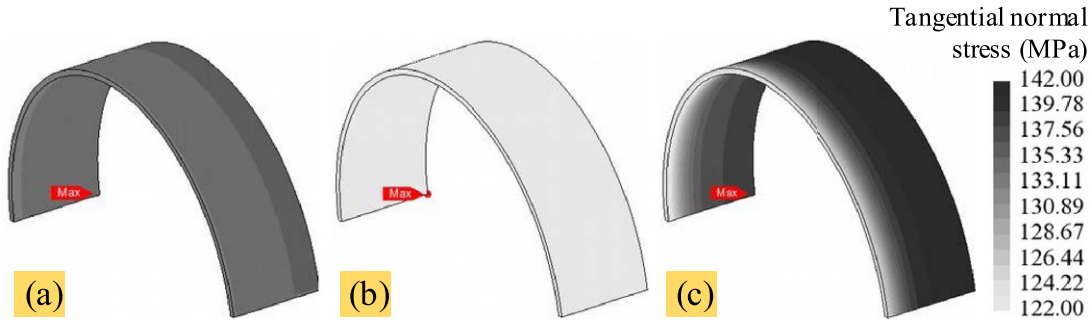

Fig. 16. Tangential global stress in sleeve. (a) Condition I. (b) Condition II. (c) Condition III.

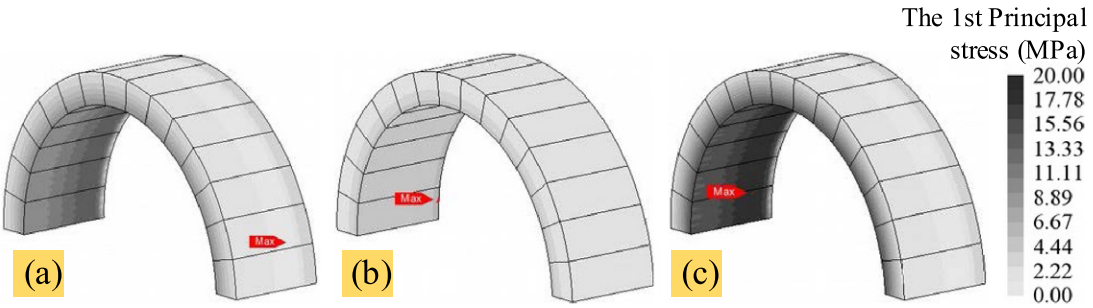

Fig. 17. The 1st principal stress in magnet. (a) Condition I. (b) Condition II. (c) Condition III.

the calculated value, which may result from the terminal contact resistance or underestimated end winding length.

The static and cogging torques are measured using a high-precision transducer, where two dc current supplies are used to avoid uneven current distribution, due to the difference in phase resistance. The peak-to-peak cogging torque is 0.06 Nm and larger than the calculated value, as in Fig. 21. Figure 22 shows the average torques with different currents, and nearly linear variations are observed, which are well-aligned with the fact that magnetic saturation in the stator core is negligible. In addition, the measured torques

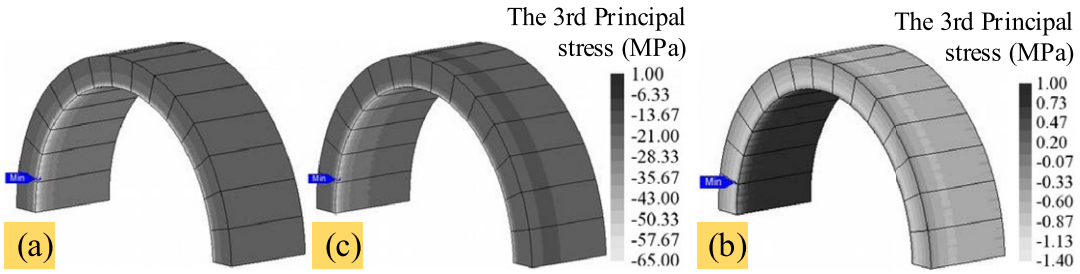

Fig. 18. The 3rd principal stress in magnet. (a) Condition I. (b) Condition II. (c) Condition III.

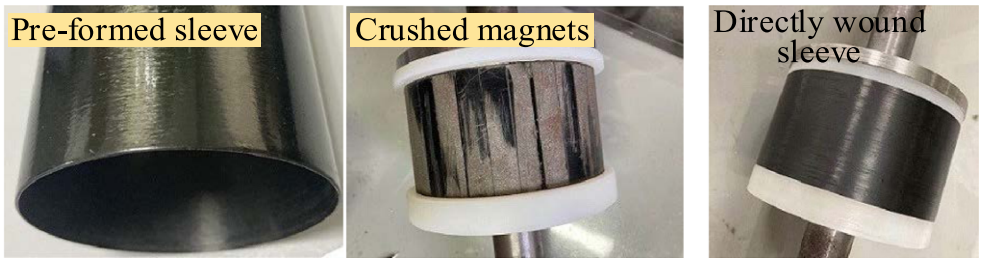

Fig. 19. Directly wound and pre-formed carbon fiber composite sleeves.

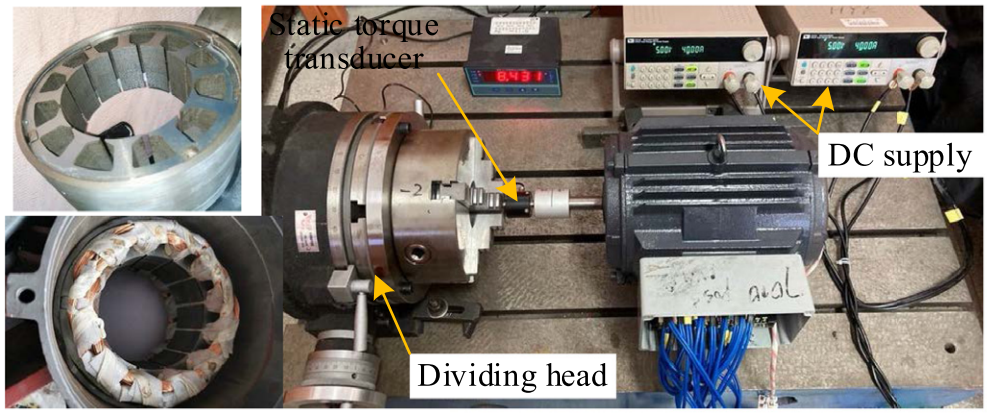

Fig. 20. Stator assembly and setups for static torque measurement.

Table 8
Phase resistance and inductance

Parameter	Calculated	Measured	Error (%)
Resistance R_p (Ω)	0.0252	0.0295	14.5
Inductance L_p (mH)	87.94	91.92	4.57

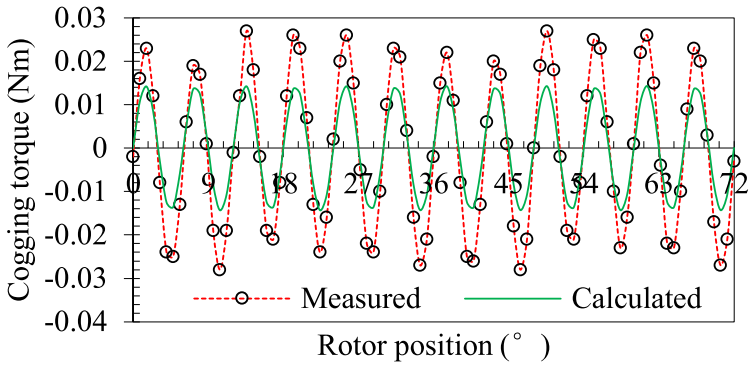

Fig. 21. Calculated and measured cogging torque waveforms.

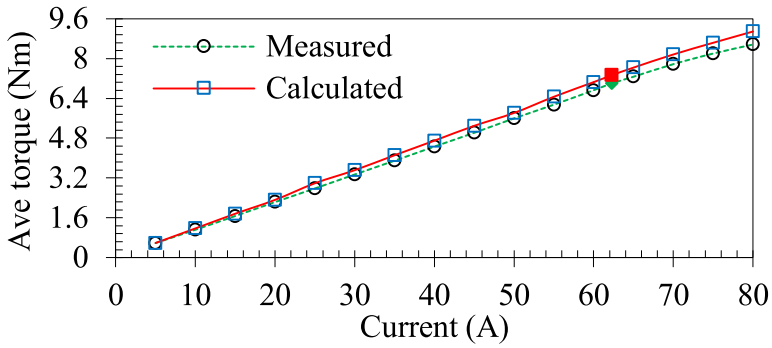

Fig. 22. Average output torques against different line currents.

are slightly smaller than the calculated ones, but the maximum error is only 3.50% which is acceptable considering manufacturing or material tolerance.

A back-to-back platform is built for open-circuit and on-load tests, as shown in Fig. 23. Below 8000 r/min, a torque transducer HCNJ-101 is used. Whereas, at a higher speed, the motor and generator are directly connected to increase the first critical speed. Figure 24 shows the measured back EMF and comparisons to the simulations. The peak EMF is measured to be 203.5 V and slightly smaller than the predicted one of 206.94 V, which is conceivably attributed to the degraded magnets. However, due to the nature of tooth-coil winding, the back EMF of 10P12s is approximately sinusoidal, with low harmonic distortion.

On-load performances are evaluated using the common dc bus inverter units, where the switching frequency is fixed to 10 kHz. Figure 25 are the measured and calculated phase currents at the rated point. In this case, the fundamental frequency reaches 1250 Hz with a carrier ratio of 8. It can be seen that, though with a low carrier ratio, the current ripple is effectively suppressed due to a larger winding inductance, which as aforementioned owes mainly to the stator leakage inductance and harmonic leakage inductance. In addition, the rotor integrity is stably kept at the maximum speed of 15000 r/min, verifying that the rotor design has sufficient strength.

Due to the difficulty of separating each loss component and the poor prediction accuracy of the bearing and windage loss, the calculated stator iron loss P_{Fe}, copper loss P_{co}, and rotor eddy current loss P_{ed} are indirectly validated, by measuring the sum of them, i.e., the electromagnetic loss P_{ma}. This method uses

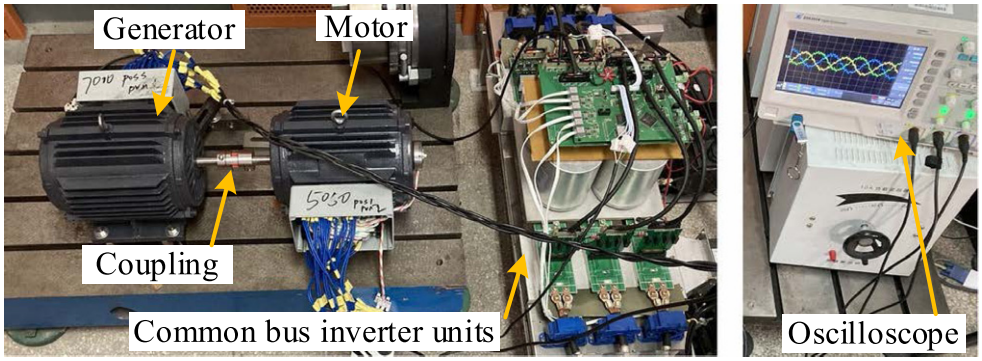

Fig. 23. Setups for open-circuit and on-load tests above 8000 r/min.

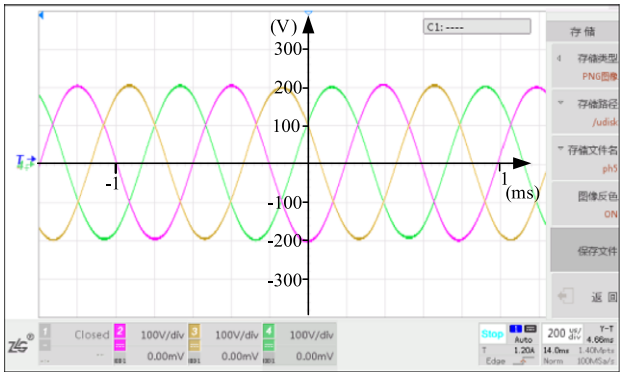

(a) Measured line-line back EMF

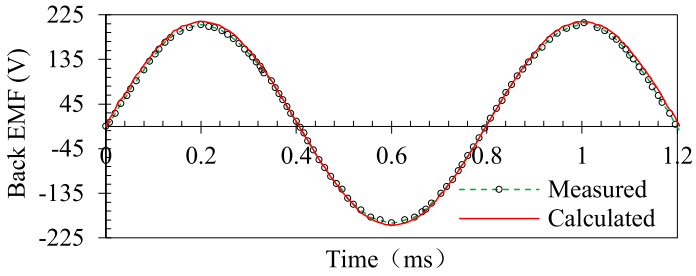

(b) Calculated line EMF using 3D-FEA

Fig. 24. Measured and calculated back EMFs at 14986 r/min.

a torque meter to measure the transferred shaft torque T_{sh} and power P_{sh}, as in (7). The generator power P_e is measured using a power analyzer, as in (8).

$$P_{sh} = \frac{2\pi n T_{sh}}{60} \tag{7}$$

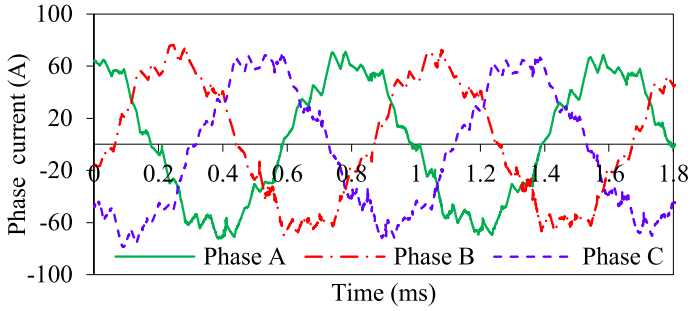

(a) Phase current using filed-control co-simulation

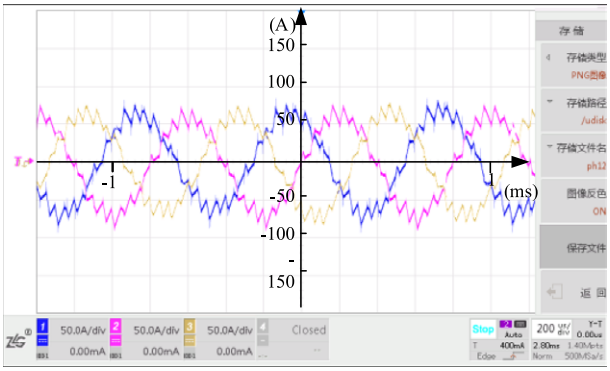

(b) Measured phase current

Fig. 25. Measured and calculated phase current at the rated operating point.

Table 9
Calculated and measured loss results

Test	P_m (W, meas)	P_e (W, meas)	P_{oc} (W, meas)	P_{ma} (W, meas)	P_{ma} (W, calc)	Error (%)
Open-circuit (dummy rotor)		0	139.25	–	–	–
Open-circuit (real rotor)	139.25	0	384.37	245.12	221.37	10.73
On-load (real rotor)		5835.5	6268.36	293.61	265.54	10.57

$$P_{sh} = \overbrace{P_{af} + P_{br}}^{P_m} + P_e + \overbrace{P_{Fe} + P_{co} + P_{ed}}^{P_{ma}}. \tag{8}$$

To separate the mechanical loss P_m, a dummy rotor for the generator with unmagnetized magnets is built and driven by the motor. In this case, the shaft power P_{sh} contains only the bearing friction loss P_{br} and the windage loss P_{af}. Assuming P_m for the dummy and magnetized rotors are identical, and subtracting P_m and P_e from P_{sh}, electromagnetic loss P_{ma} is obtained. Measured losses at 7992 r/min are listed in

Table 9. The calculated P_{ma} is close to the measured result on both the open-circuit and load conditions, with the maximum error at 10.73%, which validates the loss calculation methods.

7. Conclusions

In this paper, the feasibility study on using tooth-coil PMSM in motorized spindle is fully explored for increased rigidity, efficiency, and further system miniaturization. Benchmarking the original solution with conventional distributed winding, a TC-PMSM is designed and comparatively analyzed. It is found that by using tooth-coil winding, the axial length of the rotor is reduced, and in turn increases the spindle's rigidity. Meanwhile, TC-PMSM has a larger inductance that helps to downsize the filters of the inverter. Moreover, though with a higher frequency, all electromagnetic losses of the spindle are reduced, leading to higher efficiency and expected smaller thermal elongation. In addition, by simulations and full-scale experimental results, the strength and magnetization are well kept for the rotor with bonded magnets, demonstrating the proposed configuration is promising and feasible for a high-power spindle system.

Acknowledgements

This work was supported in part by the National Natural Science Foundation of China (52307058), in part by the Natural Science Foundation of Jiangsu Province (BK20230322), and in part by the Natural Science Foundation of the Higher Education Institutions of Jiangsu Province, China (23KJB470011).

References

[1] H. Zhao, S. Yu and F. Sun, Harmonic suppression and torque ripple reduction of a high-speed permanent magnet spindle motor, *IEEE Access* **9** (2021), 51695–51702.
[2] G. Du, N. Huang, Y. Zhao, G. Lei and J. Zhu, Comprehensive sensitivity analysis and multiphysics optimization of the rotor for a high speed permanent magnet machine, *IEEE Trans. Energy Convers.* **36**(1) (2021), 358–367.
[3] J. Hey, T.C. Sing and T.J. Liang, Sensor selection method to accurately model the thermal error in a spindle motor, *IEEE Trans. Ind. Inform.* **14**(7) (2018), 2925–2931.
[4] S.J. Sung, G.H. Jang, J.W. Jang, J.Y. Song and H.J. Lee, Vibration and noise in a HDD spindle motor arising from the axial UMF ripple, *IEEE Trans. Magn.* **49**(6) (2023), 2489–2494.
[5] Q. Chen, G. Li, Z. Qian, W. Cao and Q. Wang, Analysis of winding MMF of PMSM with multi-phase and multi-layer layout using holospectrum method, *International Journal of Applied Electromagnetics and Mechanics* **68**(4) (2022), 387–403.
[6] L. Fejérvári, S. Bilicz, S. Gyimóthy, J. Pávó, G. Varga et al., Electromagnetic modeling of coils made of twisted litz wire by combining finite element simulation and circuit laws, *International Journal of Applied Electromagnetics and Mechanics* **70**(1) (2022), 21–31.
[7] Y. Yao, Y. Huang, F. Peng and J. Dong, A sliding-mode position estimation method with chattering suppression for LCL-equipped high-speed surface-mounted PMSM drives, *IEEE Trans. Power Electron.* **37**(2) (2022), 2057–2071.
[8] X. Deng, M.A.S. Mohamed, S. Lambert and B. Mecrow, Development of a high-speed, permanent magnet, SiC-based drive with integrated input filters, *IEEE Trans. Energy Convers.* **35**(2) (2020), 863–874.
[9] S. Ueno, M. Enokizono, Y. Mori and K. Yamazaki, Vector magnetic characteristics of ultra-thin electrical steel sheet for development of high-efficiency high-speed motor, *IEEE Trans. Magn.* **53**(11) (2017), 1–4.
[10] W. Tong, S. Li, R. Sun, L. Sun and R. Tang, Modified core loss calculation for high-speed pmsms with amorphous metal stator cores, *IEEE Trans. Energy Convers.* **36**(1) (2021), 560–569.
[11] S. Kajii, M. Takemoto, T. Jikumaru, F. Suzuki, S. Ogasawara and K. Orikawa, Reduction in eddy current loss of concentrated windings in high-power density IPMSM using rectangular windings, in: *2021 22nd IEEE International Conference on Industrial Technology (ICIT)*, Vol. 1, IEEE, 2021, pp. 221–227..

[12] A. Bardalai, D. Gerada, D. Golovanov, Z. Xu, X. Zhang, J. Li et al., Reduction of winding AC losses by accurate conductor placement in high frequency electrical machines, *IEEE Trans. Ind. Appl.* **56**(1) (2019), 183–193.
[13] F. Wu, A. M. EL-Refaie and A. Al-Qarni, Additively manufactured hollow conductors integrated with heat pipes: Design tradeoffs and hardware demonstration, *IEEE Trans. Ind. Appl.* **57**(4) (2021), 3632–3642.
[14] S.G. Min, Modeling, investigation, and minimization of AC winding loss in slotless pm machines, *IEEE Trans. Energy Convers.* **36**(3) (2021), 2249–2260.
[15] G. Heins, D.M. Ionel and M. Thiele, Winding factors and magnetic fields in permanent-magnet brushless machines with concentrated windings and modular stator cores, *IEEE Trans. Ind. Appl.* **51**(4) (2015), 2924–2932.
[16] K. Wang, Z.Q. Zhu and G. Ombach, Synthesis of high performance fractional-slot permanent-magnet machines with coil-pitch of two slot-pitches, *IEEE Trans. Energy Convers.* **29**(3) (2014), 758–770.
[17] M.S. Islam, R. Mikail, M.A. Kabir and I. Husain, Torque ripple and radial force minimization of fractional-slot permanent magnet machines through stator harmonic elimination, *IEEE Trans. Transp. Electrification* **8**(1) (2022), 1072–1084.
[18] S. Zhu, J. Ji, W. Zhao, J. Zheng, Y. Mao and G. Liu, Unequal teeth design to reduce electromagnetic vibration in fractional-slot concentrated-windings permanent-magnet machine, *J. Magn.* **24**(4) (2019), 657–667.
[19] A. Tessarolo, C. Ciriani, M. Bortolozzi, M. Mezzarobba and N. Barbini, Investigation into multi-layer fractional-slot concentrated windings with unconventional slot-pole combinations, *IEEE Trans. Energy Convers.* **34**(4) (2019), 1985–1996.
[20] G. Dajaku, W. Xie and D. Gerling, Reduction of low space harmonics for the fractional slot concentrated windings using a novel stator design, *IEEE Trans. Magn.* **50**(5) (2014), 1–12.
[21] M.R. Shah and A.M. EL-Refaie, Eddy-current loss minimization in conducting sleeves of surface PM machine rotors with fractional-slot concentrated armature windings by optimal axial segmentation and copper cladding, *IEEE Trans. Ind. Appl.* **45**(2) (2009), 720–728.
[22] G. Choi and T.M. Jahns, Reduction of eddy-current losses in fractional-slot concentrated-winding synchronous PM machines, *IEEE Trans. Magn.* **52**(7) (2016), 1–4.
[23] S. Park, J. Lee and J. Lee, Multi-material topology optimization of permanent magnet synchronous motors, *International Journal of Applied Electromagnetics and Mechanics* **67**(4) (2021), 461–472.
[24] L. Wu, R. Qu and D. Li, Reduction of rotor eddy-current losses for surface PM machines with fractional slot concentrated windings and retaining sleeve, *IEEE Trans. Magn.* **50**(11) (2014), 1–4.
[25] Y. Wang, Z.-Q. Zhu, J. Feng, S. Guo, Y. Li and Y. Wang, Rotor stress analysis of high-speed permanent magnet machines with segmented magnets retained by carbon-fibre sleeve, *IEEE Trans. Energy Convers.* **36**(2) (2021), 971–983.
[26] P. Arumugam, Z. Xu, A.L. Rocca, G. Vakil, M. Dickinson et al., High-speed solid rotor permanent magnet machines: Concept and design, *IEEE Trans. Transp. Electrification* **2**(3) (2016), 391–400.
[27] I. Petrov, P. Lindh, M. Niemelä, E. Scherman, O. Wallmark and J. Pyrhönen, Investigation of a direct liquid cooling system in a permanent magnet synchronous machine, *IEEE Trans. Energy Convers.* **35**(2) (2020), 808–817.
[28] A. Acquaviva, S. Skoog and T. Thiringer, Design and verification of in-slot oil-cooled tooth coil winding pm machine for traction application, *IEEE Trans. Ind. Electron.* **68**(5) (2021), 3719–3727.
[29] H. Vansompel and P. Sergeant, Extended end-winding cooling insert for high power density electric machines with concentrated windings, *IEEE Trans. Energy Convers.* **35**(2) (2020), 948–955.
[30] W. M. Arshad, H. Lendenmann and H. Persson, End-winding inductances of MVA machines through FEM computations and IEC-specified measurements, *IEEE Trans. Ind. Appl.* **44**(6) (2008), 1693–1700.
[31] D.P. Kulkarni, G. Rupertus and E. Chen, Experimental investigation of contact resistance for water cooled jacket for electric motors and generators, *IEEE Trans. Energy Convers.* **27**(1) (2012), 204–210.
[32] D. Staton, A. Boglietti and A. Cavagnino, Solving the more difficult aspects of electric motor thermal analysis in small and medium size industrial induction motors, *IEEE Trans. Energy Convers.* **20**(3) (2005), 620–628.
[33] B. Sham, K. Manisekar, A.P. Senthil Kumar and D. Rajenthirakumar, Experimental study of thermal contact resistance in hardened bearing surfaces, *Exp. Heat Transf.* **28** (2015), 189–203.